Earthquake Rupture Stalled by a Subducting Fracture Zone

D. P. Robinson,* S. Das, A. B. Watts

We showed that the rupture produced by the great Peru earthquake (moment magnitude 8.4) on 23 June 2001 propagated for ~70 kilometers before encountering a 6000-square-kilometer area of fault that acted as a barrier. The rupture continued around this barrier, which remained unbroken for ~30 seconds and then began to break when the main rupture front was ~200 kilometers from the epicenter. The barrier had relatively low rupture speed, slip, and aftershock density as compared to its surroundings, and the time of the main energy release in the earthquake coincided with the barrier's rupture. We associate this barrier with a fracture zone feature on the subducting oceanic plate.

In the past three decades, the complexity of the earthquake rupture process arising from the variation of the material properties on the fault, and the effect of this variation on earthquake rupture speed and ground motion, have been extensively studied theoretically (*1*–*4*). Such studies have suggested that earthquakes can propagate around or jump over relatively strong patches ("barriers") on the fault and continue to rupture. The increased stress on these patches caused by the rupture of surrounding regions can cause the patches themselves to rupture, if the critical stress required for failure is reached, while a dynamic fracture still continues on other parts of the fault. Examples of barriers both large (≈ 1500 km^2) and small (≈ 50 km^2) that remain unbroken at the end of the dynamic rupture process are known (*5*, *6*), but the actual phenomenon of rupture around large barriers that then rupture during the earthquake has never previously been seen. In this study, we present an observation of this phenomenon from the great [moment magnitude (M_w) 8.4] Arequipa, Peru, earthquake on 23 June 2001.

At the time of its occurrence, this earthquake was the largest in magnitude to occur worldwide since 1965 and remains the third largest since then. It occurred in a ~1000-km-long seismic gap on the plate boundary where the Nazca plate subducts under the South American plate, and it caused extensive damage in nearby population centers with a large local tsunami that was observed throughout the Pacific (*7*). The 2001 earthquake only partially filled the rupture zone of the 1868 earthquake. The remaining unbroken region, together with the rupture zone of the 1877 earthquake immediately to its south, remains one of the world's major seismic gaps (Fig. 1), a 600-km zone with the potential to have a M_w 9 earthquake and generate a large tsunami. Historically, great earthquakes have occurred both to the immediate north (for example, in 2001 and 1868) and south (for example, in 1877) of the Arica Bend. Thus, there is at least one example in the seismic cycle of these two zones being coupled (*8*, *9*).

The aftershocks of the 2001 earthquake, which we have relocated, using the method of joint hypocenter location (*9*) (figs. S1 and S2), suggest the presence of an essentially unilateral rupture extending from northwest to southeast, over a rectangular zone ~400 km by 150 km in area, and striking at 300° to 310°. We analyzed broadband seismograms, openly available from the Federation of Digital Seismic Networks, to recover the rupture process details, using the method developed by Das and Kostrov (*9*–*11*). The fault area, source time, and integral equation relating seismograms to the fault slip rate were discretized, leading to a system of linear equations. Constraints such as "positivity" (that is, no back-slip is permitted on the fault) were used to stabilize the problem, which was solved using the method of linear programming.

Our preferred solution (*9*) shows that the earthquake has a complex rupture history (Figs. 2 and 3 and movie S1). The unilateral rupture initially propagates ~70 km to the southeast and then circumvents a ~6000-km^2 barrier, after which it continues propagating farther to the southeast. At ~48 s after initiation, although the earthquake rupture is 180 km in length along strike, it has reached less than 15% of its seismic moment (*9*). About 54 s after initiation, the initially unbroken barrier commences rupturing and its rupture induces a large slip in the vicinity of the barrier, particularly in the shallow regions updip of it. The barrier ruptures completely in ~36 s at an average speed of ~2.8 km/s, which is lower than the average rupture speed of ~3.5 km/s (the local shear wave speed in the medium) over the rest of the fault. The initially unbroken barrier is also a region of relatively lower slip. About 200 km southeast of the hypocenter, a second barrier is encircled entirely by the rupture between ~36 to 60 s and breaks soon thereafter. The time of the major moment pulse, seen ~66 s after rupture initiation in the moment-rate function (inset, Fig. 3), is associated primarily with the rupturing of the first barrier and to a lesser degree with that of the second. The first barrier is a very robust feature of our solution that fits the data well (*9*). The second barrier is less well-constrained than the first because of its smaller size and later timing in the rupture process. It is important to point out that models that include a healing front behind which no further slip is permitted, and thereby constrain the rupture to occur only within a prescribed rupture front and the healing front, cannot reproduce the behavior of ruptures in which initially unbroken regions break at substantially later times, as that which occurred in this earthquake.

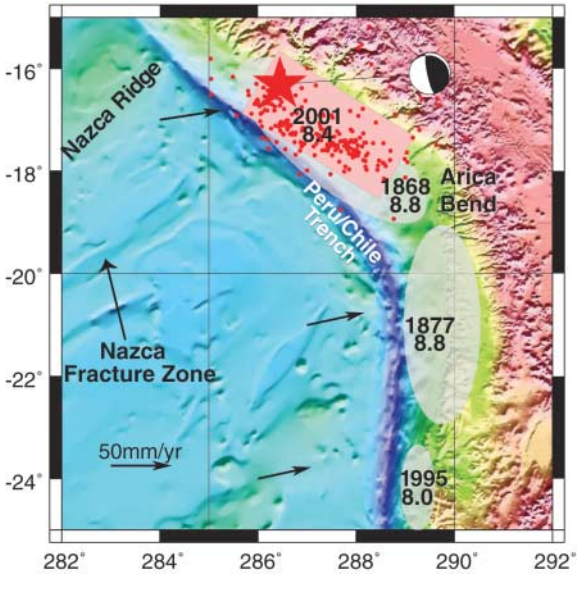

Fig. 1. Tectonic setting of the 2001 Peru earthquake, with bathymetry constructed from a General Bathymetric Chart of the Ocean (GEBCO) 1′ × 1′ grid (*24*). The shading of the bathymetry shows its slope in the direction of an artificial sun at an azimuth of 160° (dark shades represent gentle slopes, light shades represent steep slopes). Black arrows show the plate motion vectors of the Nazca plate relative to the South American plate. Approximate rupture zones of known great (magnitude ≥ 8.0) earthquakes in the region since the mid-19th century (*8*) are shown as light ovals, labeled with magnitude and year of occurrence. The rupture zone of the 2001 earthquake is shown as a red rectangle, and its epicenter is depicted by a red star. Red dots denote the aftershocks, which have been relocated, observed for 24 hours after the main earthquake (*9*). The centroid-moment tensor solution (*9*) is plotted as a black and white circle. The Nazca Ridge and Arica Bend are marked in place and a black arrow points to the location of the Nazca Fracture Zone, the subduction of which leads to the rupture complexity of this earthquake.

Department of Earth Sciences, University of Oxford, Parks Road, Oxford, OX1 3PR, UK.

*To whom correspondence should be addressed. E-mail: David.Robinson@earth.ox.ac.uk

To determine the cause of the barriers, we have examined the available marine geophysical data (*12*–*16*) in the region of the subducting oceanic plate. The oceanic crust immediately adjacent to the earthquake rupture zone is 45 to 50 million years old and was generated by seafloor spreading at the fossil Pacific/Farallon ridge. Despite relatively fast half-spreading rates (~50 mm/year), the bathymetry is not smooth but is complex and in places highly irregular. The most notable bathymetric feature is a 25- to 50-km-wide ridge that rises to ~700 m above the expected depth of the oceanic crust (Fig. 3), flanking a 20- to 25-km-wide trough that is up to ~300 m deeper than the expected depth. The ridge and trough are separated by a distinctive southeast-facing scarp that can be traced from the seaward wall of the trench in the northeast, across the outer rise, to the Nazca Fracture Zone in the southwest (*15*), a distance of some 275 km (Figs. 1 and 3 and fig. S4). The ridge, scarp, and trough features resemble an oceanic fracture zone and may represent either a northeastern extension of the Nazca Fracture Zone (*16*) or some form of fracture that developed in the plate as a response to slab-induced plate boundary forces (*17*). Irrespective of its origin, the fracture zone feature aligns very well with the first barrier and, we suggest, increases the coupling between the two sides of the fault, resulting in the highly heterogeneous earthquake rupture history. The nonuniformity of the aftershock distribution (Fig. 1 and figs. S1 and S2) over the fault mirrors the complexity of the rupture history. In fact, the trapezoidal shape of the first barrier (Fig. 2), which has relatively low slip, coincides with a trapezoidal region of lower aftershock density, visible both in the 24-hour and the 6-month aftershock distributions. This finding contrasts with the usual observation that regions of higher slip have fewer aftershocks (*18*).

The fracture zone feature can be traced on ship track profiles conducted over large distances, which show variations between profiles (of up to several hundreds of meters) in the amplitude of the ridge and trough (fig. S5). We suggest that the higher slip in the shallower depth in this part of the fault reflects a morphologically more subdued segment of the fracture zone feature. The cause of the second barrier is not as clear. Available bathymetric data suggest that there is no fracture zone feature on the subducting oceanic crust immediately seaward of the second barrier. There are, however, a number of large seamounts in the region (such as seamount X on mw853 in Fig. 3), and we speculate that such a feature may be the cause of the second barrier.

The notion that subduction of bathymetric features increases the seismic coupling on the subduction zone has been suggested by a number of previous workers (*19*–*21*), and specific examples related to seamount subduction (*21*) have been discussed. The influence of subducting bathymetric features on the behavior of earthquake ruptures is important in the context of truly great earthquakes, such as the M_w 9.1 and the M_w 8.7 earthquakes of 2004 and 2005 in Sumatra (*22*), where segmentation of the plate boundary caused these two earthquakes to occur 3 months apart. If these two had occurred as one even larger earthquake, its effects would have been even more catastrophic. The physical origin of this segmentation is unknown but is likely to be due to features on the subducting oceanic plate.

The results of this study have important implications for our understanding of the principles of the mechanics of earthquakes, because the time delay of ruptures at barriers can be used to estimate fracture energy (*3*), which is a measure of fault strength. They also shed light on how ruptures propagate through materials with non-uniform strength properties, which is relevant to the understanding of fracture in all materials for engineering applications (*2*). Finally, such rupture complexity also has a profound influence on the ground shaking, and hence damage, caused by earthquakes, because high-frequency damaging waves are generated when the rupture changes speed (*3*, *23*).

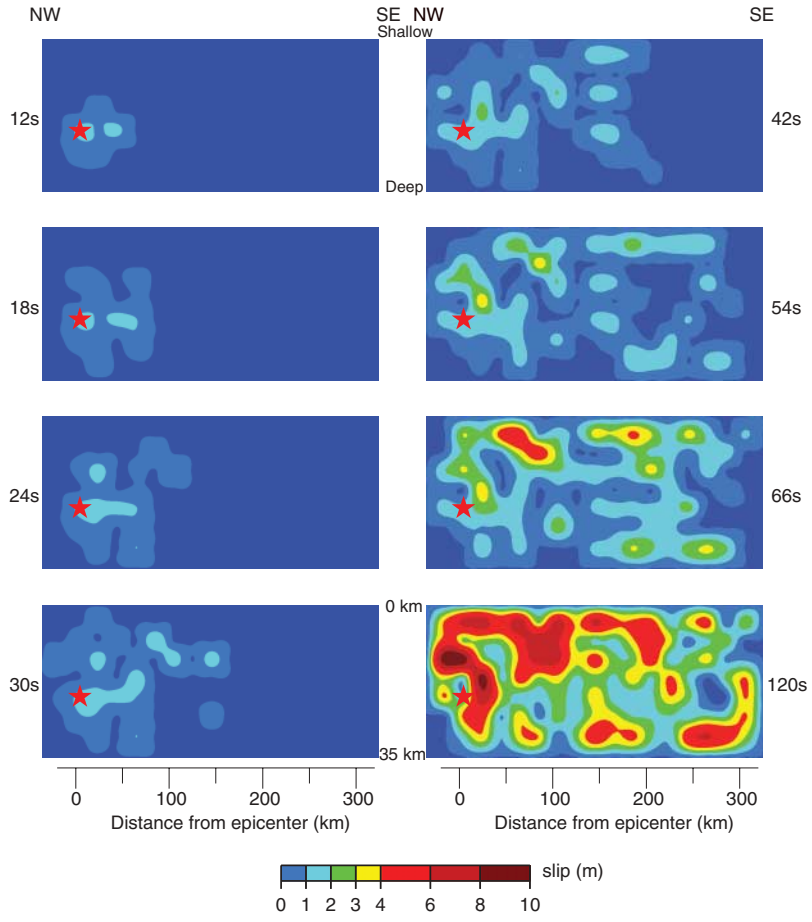

Fig. 2. Frames showing the dynamic rupture process for our preferred solution (*9*) at selected times marked on the side of each frame. See movie S1 for the full rupture history. The slip contours are plotted on the rectangular fault, which is viewed from the fault-normal direction. In each rectangle, the height represents fault depth from top (shallow edge, 0 km depth) to bottom (deep edge, ~35 km depth), and the width represents direction from left (northwest) to right (southeast). The left edge of the barrier, located ~70 km from the epicenter, is seen from 12 to 42 s, and its trapezoidal shape is seen at 42 s. Slip on the barrier starts at 48 s (movie S1) and is seen at 54 s. The rupture of the barrier induces a large slip (red) at shallow depth. For the comparison of data with solution synthetics, see the supporting online material (SOM) (fig. S3). The average slip over the fault was ~3.5 m, giving an average stress drop of ~0.8 MPa. The average slip in the region of the first barrier was ~2.8 m.

References and Notes

1. B. V. Kostrov, S. Das, *Principles of Earthquake Source Mechanics* (Cambridge Univ. Press, New York, 1988).
2. L. B. Freund, *Dynamic Fracture Mechanics* (Cambridge Univ. Press, New York, 1990).
3. M. T. Page, E. M. Dunham, J. M. Carlson, *J. Geophys. Res.* **110**, B11302 (2005).
4. S. Das, K. Aki, *J. Geophys. Res.* **82**, 5658 (1977).
5. C. Henry, S. Das, J. H. Woodhouse, *J. Geophys. Res.* **105**, 16097 (2000).
6. K. B. Olsen, R. Madariaga, R. J. Archuleta, *Science* **278**, 834 (1997).
7. A. Rodriguez-Marek, C. Edwards, Eds. *Southern Peru Earthquake of 23 June 2001 Reconnaissance Report,* special issue of *Earthquake Spectra* **19**, (2003).

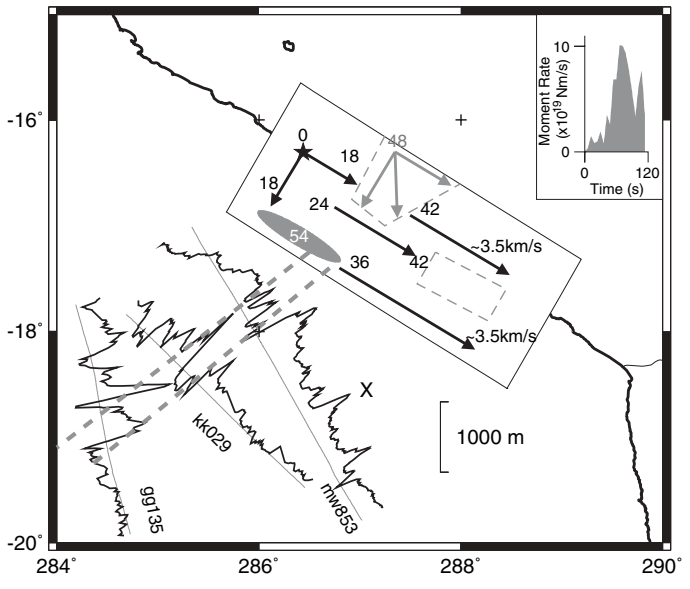

Fig. 3. Schematic representation of the rupture process. The epicenter is indicated by a black star. The two barriers are delineated by thin gray dashed lines within the central rectangle. Arrows showing earthquake rupture direction are labeled with start and selected end times (in seconds) of segments. Arrow color indicates the primary rupture (black) and the rupture of barriers (gray). Approximate rupture speeds (kilometers per second) are also indicated. The solid gray oval, shallower than the first barrier, indicates the region of high shallow slip induced by the rupture of this barrier, with the number indicating start time (54 s) when this shallow slip was induced. The three jagged black lines show the residual bathymetry (the observed bathymetry minus the bathymetry expected for the age of the oceanic crust) projected orthogonally onto ship tracks shown as three thin gray lines. Ship tracks (mw853, kk029, and gg135) are labeled according to their cruise identification in the Geophysical Data System database. The black X on bathymetric profile mw853 represents the location of a seamount. The two thick gray dashed lines show the ridge and trough features that can be correlated on each ship track (see the SOM for more details), interpreted in this study to be the physical origin of the large barrier that stalls the earthquake. The graph (inset, top right) depicts the moment-rate function.

8. D. Comte, M. Pardo, *Nat. Hazards* **4**, 23 (1991).
9. Materials and methods are available as supporting material on *Science* Online.
10. S. Das, B. V. Kostrov, *J. Geophys. Res.* **95**, 6899 (1990).
11. S. Das, B. V. Kostrov, *Phys. Earth Planet. Inter.* **85**, 293 (1994).
12. E. M. Herron, *Geol. Soc. Am. Bull.* **83**, 1671 (1972).
13. W. J. Schweller, L. D. Kulm, R. A. Prince, in *Nazca Plate: Crustal Formation and Andean Convergence, A Volume Dedicated to George P. Woollard*, L. D. Kulm, J. Dymond, E. J. Dasch, D. M. Hussong, Eds. (Geological Society of America, Boulder, CO, 1981), pp. 323–350.
14. A. V. Judge, M. K. McNutt, *J. Geophys. Res.* **96**, 16625 (1991).
15. D. W. Handschumacher, in *Geophysics of the Pacific Ocean Basin and Its Margin, A Volume in Honor of George P. Woollard*, G. H. Sutton, M. H. Manghnani, R. Moberly, Eds. (American Geophysical Union, Washington, DC, 1976), pp. 177–202.
16. S. C. Cande *et al.*, *Magnetic Lineations of the World's Ocean Basins, Scale 1:27,400,000* (map, *American Association of Petroleum Geologists*, Tulsa, OK, 1989).
17. S. Cloetingh, R. Wortel, *Tectonophysics* **132**, 49 (1986).
18. S. Das, C. Henry, *Rev. Geophys* **41**, 10.1029/2002RG000119 (2003).
19. J. Kelleher, W. McCann, *J. Geophys. Res.* **81**, 4885 (1976).
20. M. Cloos, *Geology* **20**, 601 (1992).
21. C. H. Scholz, C. Small, *Geology* **25**, 487 (1997).
22. R. Bilham, *Science* **308**, 1126 (2005).
23. R. Madariaga, *Geophys. J. R. Astron. Soc.* **51**, 625 (1977).
24. British Oceanographic Data Centre, *The GEBCO Digital Atlas*, Centenary Edition (CD-ROM) (Liverpool, UK, 2003).

25. D.P.R. is supported by a U.K. Natural Environmental Research Council (NERC) studentship NER/S/A/2003/11309 and a Schlumberger Cooperative Awards in the Sciences of the Environment (CASE) grant. The work is supported in part by NERC grant NE/C518806/1.

Supporting Online Material

www.sciencemag.org/cgi/content/full/312/5777/1203/DC1
Materials and Methods
Figs. S1 to S5
References
Movie S1

3 February 2006; accepted 7 April 2006
10.1126/science.1125771

Reduced Radiative Conductivity of Low-Spin (Mg,Fe)O in the Lower Mantle

Alexander F. Goncharov,* Viktor V. Struzhkin, Steven D. Jacobsen†

Optical absorption spectra have been measured at pressures up to 80 gigapascals (GPa) for the lower-mantle oxide magnesiowüstite (Mg,Fe)O. Upon reaching the high-spin to low-spin transition of Fe^{2+} at about 60 GPa, we observed enhanced absorption in the mid- and near-infrared spectral range, whereas absorption in the visible-ultraviolet was reduced. The observed changes in absorption are in contrast to prediction and are attributed to *d-d* orbital charge transfer in the Fe^{2+} ion. The results indicate that low-spin (Mg,Fe)O will exhibit lower radiative thermal conductivity than high-spin (Mg,Fe)O, which needs to be considered in future geodynamic models of convection and plume stabilization in the lower mantle.

Silicate perovskite $(Mg,Fe)SiO_3$ and magnesiowüstite (Mg,Fe)O are the major constituents of Earth's lower mantle. Because of partially filled *d*-electron orbitals, the presence of Fe in these minerals strongly influences the radiative component of conduction and thus their ability to transfer heat effectively (*1*). Pressure- and temperature-dependent thermal conductivity of minerals (*2*, *3*) is now thought to control some aspects of mantle convection and plume stability (*4*–*7*). In addition to the presence of large so-called superplumes (*8*, *9*), the complex seismic structure of Earth's lower mantle also reveals lateral heterogeneities that have been explained by compositional and thermal variation, partial melting, and phase transformations (*10*–*13*). The recent discovery of a spin-pairing high-spin (HS) to low-spin (LS) electronic transition of iron in silicate perovskite (*14*) and magnesiowüstite (*15*) have also been invoked to explain these anomalies. In (Mg,Fe)O, the HS-LS transition between 50 and 70 GPa strongly influences its bulk elastic properties (*16*, *17*) and is expected to blue-shift iron absorption bands in the infrared (IR) (*1*, *18*), although the transport properties of low-spin (Mg,Fe)O at high pressure have remained only speculative. Here, we provide experimental evidence for reduced radiative conductivity in LS-(Mg,Fe)O from optical absorption spectra through the spin-pairing transition in magnesiowüstite single crystals with varying iron contents spanning possible lower-mantle compositions.

Absorption spectra were obtained at pressures up to 80 GPa for high-quality single-crystal samples of $[Mg_{(1-x)}Fe_x]O$ with $x = 0.06$, 0.15, and 0.25 by a proper referencing of the transmission spectra measured through the sample (*19*) (fig. S1). The measurements were carried out in a diamond anvil cell with Ne or Ar pressure media (*19*). At low pressure, the $(Mg_{0.94}Fe_{0.06})O$ sample shows a broad absorption maximum ~8000 to 10,000 cm^{-1}, resulting from electronic transitions between Fe^{2+} d-orbitals of T_{2g} and E_g symmetry split by the crystal field, and an absorption tail in the visible-ultraviolet (UV) range that was assigned

Geophysical Laboratory, Carnegie Institution of Washington, 5251 Broad Branch Road, NW, Washington, DC 20015, USA.

*To whom correspondence should be addressed. E-mail: goncharov@gl.ciw.edu

†Present address: Department of Geological Sciences, Northwestern University, Evanston, IL 60208, USA.